Article | Open Access

Energy Materials

Zhang *et al. Energy Mater.* **2026**, *6*, 600123 **DOI:**10.20517/energymater.2026.185

Bismuth chloride additive regulated anode interphase and kinetics in manganese-ion batteries

Yuxuan Zhang#, Ying Zhang#, Shize Liu, Hexige Wuliji, Huirong Liu, Aruuhan Bayaguud*

Keywords:
Nonaqueous manganese-ion battery, electrolyte additive, interface modification, electrochemical reaction kinetics

Citation: Zhang, Y.; Zhang, Y.; Liu, S.; Wuliji, H.; Liu, H.; Bayaguud, A. Bismuth chloride additive regulated anode interphase and kinetics in manganese-ion batteries. *Energy Mater.* **2026**, *6*, 600123. https://dx.doi.org/10.20517/energymater.2026.185

Received: 25 Jun 2026 **First Decision:** 24 Jul 2026 **Revised:** 22 Aug 2026 **Accepted:** 8 Sep 2026 **Published:** 22 Sep 2026

Academic Editor: Federico Bella
Copy Editor: Fangling Lan
Production Editor: Fangling Lan

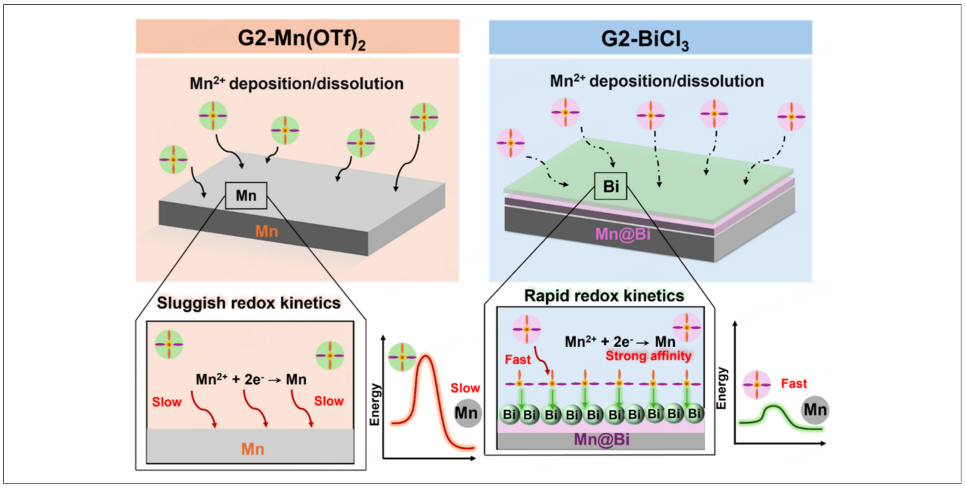

Abstract

The use of nonaqueous electrolyte in manganese-ion batteries (MIBs) has attracted increasing scientific attention because of their unique properties. These systems significantly reduce water-molecule interference in electrode reactions, effectively precluding unwanted side reactions such as the hydrogen evolution reaction, which commonly occurs in aqueous electrolytes. Nonaqueous electrolyte development is still a challenge, though. Mn^{2+} has a high charge density, which leads to sluggish Mn^{2+} kinetics and greatly limits the development of nonaqueous MIBs. In this study, $BiCl_3$ is used as an electrolyte additive to enhance the reaction kinetics of Mn^{2+} in a diglyme-based nonaqueous electrolyte. Electrochemical testing shows that the polarization voltage of Mn||Mn symmetric cells is greatly reduced following the addition of $BiCl_3$. Full characterization by X-ray diffraction and scanning electron microscopy, combined with density functional theory calculations, suggests that Bi^{3+} undergoes a spontaneous galvanic replacement reaction with the Mn anode. This process enables the *in situ* formation of a Bi-containing interphase, which helps reduce the activation barrier for charge transfer. Thus, the full cell with a $Cu_{1.8}S$ cathode delivered an improved average discharge capacity of 166.1 mAh g^{-1} over 200 cycles at 100 mA g^{-1}. This work provides perspectives for designing the interfacial chemistry of MIBs.

School of Materials Science and Engineering, Inner Mongolia University of Technology, Hohhot 010051, Inner Mongolia, China.
#Authors contributed equally.

***Correspondence to:** Prof. Aruuhan Bayaguud, School of Materials Science and Engineering, Inner Mongolia University of Technology, No. 49 Aimin Street, Xincheng District, Hohhot 010051, Inner Mongolia, China. E-mail: jinaruhan@imut.edu.cn

INTRODUCTION

The world's growing need for sustainable energy and increased awareness of the need to mitigate environmental effects have contributed to a significant shift toward electric mobility from internal combustion engine vehicles. In this context, lithium-ion batteries (LIBs) have become the cornerstones of the clean energy revolution[1-4]. But the rapid growth of electric vehicle (EV) sales has created a "staggering" need for lithium, highlighting the critical weaknesses in the supply chain. Lithium reserves are vast, but only a portion is high-quality, low-cost, and geographically concentrated. Lithium demand is forecast to grow rapidly and may not meet the demands of the global energy transition over the next decade. To overcome these problems, researchers have started investigating alternative energy storage systems, including sodium-ion batteries[5-7] and potassium-ion batteries[8,9]. At the same time, multivalent metal anodes (Mg, Ca, Zn, Cu, Fe, and Mn) have been attracting great attention because of their multi-electron transfer nature and excellent cost-effectiveness, supported by the fact that these metals are widely available on Earth. Among the different multivalent systems reported to date, such as magnesium[10,11], zinc[12-15], and aluminum-ion batteries[16,17], manganese-ion batteries (MIBs) are one of the most promising candidates[18-21].

Manganese (Mn) is a cost-effective and earth-abundant transition metal, and the reserves in the Earth's crust are more than 1.5 billion tons. Mn is the 12th most abundant element in the Earth's crust and could be a strategic option to mitigate the risks of lithium resource depletion[22,23]. Similarly, Mn is relatively stable in air and can be stored in air, which significantly lowers manufacturing, storage, and transportation costs as compared to other highly reactive metals[24]. As an anode material, Mn metal has a moderate reduction potential of -1.19 V *vs.* the standard hydrogen electrode (SHE), allowing Mn metal batteries to achieve a relatively high discharge voltage. Mn has a high specific capacity (976 mAh g^{-1}) and volumetric capacity (7,250 mAh cm^{-3}). These performance benefits demonstrate the potential applications and practical value of the Mn metal anode[25,26].

Electrolyte research on MIBs falls into two categories: aqueous and nonaqueous. Many strategies were proposed for aqueous MIBs, but the world's aqueous MIB systems are often hampered by capacity fading and shortened cycle life as a result of interfacial polarization, hydrogen evolution reaction (HER), irreversible parasitic reactions, and continuous electrolyte depletion[19,21,27]. Nonaqueous electrolytes offer a strategic advantage by significantly reducing water-related parasitic reactions compared with aqueous systems. They provide an electrochemical stability window that extends far beyond the inherent electrochemical limits of aqueous media. Recent advances have demonstrated this: He *et al.* developed an electrolyte using N, N-dimethylformamide and ethylenediamine (EDA)[22]. The symmetric cell of Mn||Mn had a minimum overpotential of 0.5 V at a current density of 0.2 mA cm^{-2}. The complexes of EDA in the electrolyte promote the desorption of Mn^{2+} and decrease the overpotential in the symmetric cell[22]. Shen *et al.* then proposed a halogen-mediated approach that introduced the first halogen-mediated nonaqueous electrolyte (HM-NAE)[24]. Cycling instability can be reduced by incorporating less electronegative Cl atoms into the first solvation shell of the Mn^{2+}, which decreased the cation-solvent interaction, resulting in > 700 h of stable cycling[24]. Zhang *et al.* further improved this with an asymmetric tetramethylene sulfone (TMS) coordinated $Mn_2(\mu\text{-}Cl)Cl_2(TMS)_x(TFSI)_n^+$ cluster electrolyte (AS-NAE), which provides higher ionic conductivity of 3.63-4.68 mS cm^{-1} and allows robust operation at -40 °C[28]. Recently, Jing *et al.* introduced a synergistic approach combining the use of an indium nitride interfacial layer and 2-methoxyethylamine additive to maximize the lifespan of symmetric cells for more than 3,400 h[29].

However, several major hurdles must be overcome before these MIBs can be used in practice. The charge density of Mn^{2+} is high, and it has a strong tendency to coordinate with solvent molecules, resulting in a high energy barrier for the desolvation process[24]. The tendency for electrode passivation leads to naturally low redox kinetics. A dense oxide film forms spontaneously on the surface of the Mn metal, resulting in a high

resistance to charge transfer between the metal and electrolyte, which further hinders the plating/stripping of Mn^{2+} ions[29]. Together, these factors contribute to high overpotentials, high polarizations, and poor cycle kinetics, which in turn greatly limit the rate capability and stability of MIBs.

To tackle these kinetic challenges, this study introduces a judicious electrolyte additive to modify the anode-electrolyte interface. The unique electronic configurations of Bi and its derivatives are highly effective in optimizing ion transport across the interfaces in different types of batteries, including sodium-ion batteries[30,31], potassium-ion batteries[32], zinc-ion batteries[33], and magnesium-ion batteries[34]. We introduced $BiCl_3$ into a basic diglyme electrolyte to create a new nonaqueous electrolyte (G2-$BiCl_3$). In this setup, a facile *in situ* chemical reaction occurs between Bi^{3+} and a Bi-containing interphase is formed on the Mn anode. Theoretical simulations and experimental characterization show that this interphase aids Mn deposition/stripping. Thus, the Mn||Mn symmetric cell can be reversibly cycled for more than 1,000 h at 0.1 mA cm^{-2}. Moreover, the full cell with a $Cu_{1.8}S$ cathode delivered a higher average discharge capacity of 166.1 mAh g^{-1} over 200 cycles at 100 mA g^{-1}, demonstrating the enhanced performance of the G2-$BiCl_3$ electrolyte. This Bi-containing interphase design provides a potent strategy for overcoming the sluggish kinetics of Mn anodes, offering new insights into interfacial engineering for high-performance MIBs.

EXPERIMENTAL

Materials

Mn(II) trifluoromethanesulfonate ($Mn(OTf)_2$, 99.5%) was obtained from Dodo Chemical Reagent Co., Ltd. Bismuth(III) chloride ($BiCl_3$, >98%), copper(II) chloride dihydrate ($CuCl_2·2H_2O$, 99.99%), thiourea (CH_4N_2S, 99%), ethylene glycol ($C_2H_6O_2$, 98%), diglyme (G2, 99.8%), and lithium chloride (LiCl, anhydrous, 99.9%) were purchased from Aladdin Biochemical Technology Co., Ltd. Manganese powder (Mn, 99.9%, 200 mesh) was supplied by Macklin Biochemical Co., Ltd. All chemicals were used as received unless otherwise specified.

Preparation of different electrolytes

AE: $Mn(OTf)_2$ was dissolved in deionized water to prepare an AE containing 0.5 M $Mn(OTf)_2$.

All G2-based electrolytes were prepared in an argon-filled glovebox (uNIVERSAL, 2440/750/900, Mikrouna, China). The electrolyte components were weighed using an analytical balance (Quintix 125D-1CN, Sartorius, China) and continuously stirred at room temperature at 200 rpm for 24 h using a magnetic stirrer (TMHB-180CL, Taisite Instrument Co., Ltd., China).

G2-$Mn(OTf)_2$: $Mn(OTf)_2$ was dissolved in G2 solvent to obtain a 0.5 M $Mn(OTf)_2$/G2 electrolyte. The solution was sealed and stirred for 24 h to ensure complete dissolution and homogeneous mixing.

G2-$Mn(OTf)_2$-$BiCl_3$: $BiCl_3$ was added to the 0.5 M $Mn(OTf)_2$/G2 electrolyte, and the mixture was stirred for 24 h. By adjusting the amount of $BiCl_3$, electrolytes with different $BiCl_3$ concentrations (5, 10, and 25 mM) were prepared and denoted as G2-5mM $BiCl_3$, G2-$BiCl_3$, and G2-25mM $BiCl_3$, respectively.

G2-$Mn(OTf)_2$-LiCl: Based on the 0.5 M $Mn(OTf)_2$/G2 electrolyte, LiCl was added to achieve a final concentration of 30 mM. After stirring for 24 h, the G2-$Mn(OTf)_2$-LiCl electrolyte (denoted as G2-LiCl for simplicity) was obtained. The LiCl concentration was selected to provide the same Cl^- concentration as that introduced by 10 mM $BiCl_3$.

Preparation of Mn anode and $Cu_{1.8}S$ cathode

Mn anode: The preparation procedure for the Mn anode in this study was based on previously reported methods[24]. Mn powder, Super P, and poly(vinylidene fluoride) (PVDF) were mixed in a weight ratio of 8:1:2, followed by adding N-methyl-2-pyrrolidone (NMP) to form a homogeneous slurry (TMHB-180CL, Taisite Instrument Co., Ltd., China; room temperature; 200 rpm for 2 h). Using a 500 μm doctor blade, the well-stirred slurry was uniformly coated onto a glass plate and dried in a vacuum oven (MSK-H200A, Hefei KJ Magnetic Electronics Co., Ltd., China) at 80 °C for 12 h. The dried electrode film was peeled off the glass plate and cut into circular electrodes with a diameter of 12 mm. The mass of each Mn anode was approximately 12-13 mg. As shown in Supplementary Figures 1 and 2, the Mn anode prepared in this study exhibits high chemical purity and good mechanical integrity, showing no cracking or powder shedding after operations such as tweezer handling and battery cell encapsulation.

$Cu_{1.8}S$ cathode: The preparation procedure for the $Cu_{1.8}S$ cathode material in this study follows the reported literature[35]. Briefly, 2.0 g $CuCl_2 \cdot 2H_2O$ (11.7 mmol) and 3.6 g thiourea (47.3 mmol) were dissolved in 80 mL ethylene glycol at 120 °C individually. Then, the two hot, transparent solutions were mixed and stirred at 300 rpm for another 5 min before transferring the yellowish solution into a 200 mL autoclave (LC-KH-200, Lichen Scientific Instruments (Hunan) Co., Ltd., China). The autoclave was sealed and heated at 140 °C for 6 h to produce the black suspension liquid, which was vacuum filtered, washed with de-ionized water and anhydrous ethanol 3 times each, and vacuum dried at 80 °C to obtain the dark gray precursor. This precursor was then sintered at 350 °C at a ramping rate of 5 °C min^{-1} in an argon atmosphere for 2 h using a tube furnace (OTF-1200X, Hefei KJ Magnetic Electronics Co., Ltd., China) and cooled to room temperature naturally to obtain the final product. To prepare the cathode slurry, 210 mg $Cu_{1.8}S$ powder, 60 mg Ketjen Black, and 30 mg PVDF were ground in a weight ratio of 7:2:1 and uniformly stirred with 3 mL NMP at 200 rpm to obtain a homogeneous slurry (TMHB-180CL, Taisite Instrument Co., Ltd., China; room temperature; 200 rpm for 2 h). The slurry was directly coated onto Cu foil, dried in an air-blowing oven (DHG-9070A, Shanghai Yiheng Scientific Instrument Co., Ltd., China) for 30 min, followed by vacuum drying for 2 h to obtain the $Cu_{1.8}S$ cathode. The cathode was cut into circular electrodes with a diameter of 12 mm, with an active material loading of 1-2 mg cm^{-2} per electrode.

Material characterization

X-ray diffraction (XRD, 2θ range: 10°-80°, Shimadzu XRD-6100) and X-ray photoelectron spectroscopy (XPS, ESCALAB250Xi, Thermo Fisher Scientific) were used to characterize the chemical composition of the Mn anode surface. Scanning electron microscopy (SEM, accelerating voltage: 20 kV, HITACHI SU8220, Japan; ZEISS 300 Carl Zeiss, Germany) was used to observe the surface morphology of the Mn electrode. High-resolution mass spectrometry (HRMS, Bruker ESI-Q-TOF MS/MS) was used to characterize the electrolyte. Ultraviolet photoelectron spectroscopy (UPS, Thermo Fisher Scientific ESCALAB Xi) was used to determine the work function and valence band maximum of the electrodes.

Electrochemical testing

All batteries were assembled in an argon-filled glovebox with moisture and oxygen levels below 0.01 ppm. The electrochemical performance was evaluated using CR2032-type coin cells in several configurations: Mn||Mn symmetric cells, Mn||Ti, Mn||Cu, and Mn||SS asymmetric cells, as well as Mn||$Cu_{1.8}S$ full cells. For the asymmetric cells, Ti foil (20 μm thick, 12 mm diameter) and Cu foil (100 μm thick, 12 mm diameter) were utilized as current collectors. Whatman GF/D glass fiber (17 mm diameter) served as the separator. Following assembly, the cells were sealed under a constant pressure of 85 kg cm^{-2} and allowed to equilibrate for at least 8 h prior to testing. Galvanostatic charge discharge (GCD) profiles were recorded using a LANHE battery testing system (CT3004A, Wuhan, China). Additionally, Cyclic voltammetry (CV) and Tafel polarization curves were obtained via an electrochemical workstation (CHI660E, Shanghai, China).

Tafel polarization curves: Three-electrode electrochemical measurements were performed using a Swagelok-type cell to evaluate the interfacial redox kinetics of the Mn anode. A pristine Mn anode or a $BiCl_3$-modified Mn anode was used as the working electrode, while an untreated Mn anode was used as both the counter and reference electrodes. The $BiCl_3$-modified Mn anode was obtained after cycling in the G2-$BiCl_3$ electrolyte, followed by rinsing with G2 and drying. To eliminate the direct contribution of $BiCl_3$ or dissolved Bi-containing species in the electrolyte, all three-electrode measurements were conducted in the G2-$Mn(OTf)_2$ electrolyte without $BiCl_3$. Prior to the measurements, the cells were allowed to equilibrate at the open-circuit potential for 30 min. Tafel measurements were subsequently performed at a scan rate of 0.001 V s^{-1}. All electrochemical measurements were conducted at a controlled temperature of 28 °C.

Density functional theory (DFT) calculations

All spin-polarized DFT calculations were performed by employing the Vienna ab initio simulation package. The exchange-correlation interaction was described using the Perdew-Burke-Ernzerhof functional within the generalized gradient approximation. Grimme's DFT-D3 method was used to treat van der Waals interactions. The Brillouin zone was sampled using a 3 × 3 × 1 k-point grid, and the plane-wave energy cutoff was set to 400 eV. The convergence criteria were set to 10-5 eV for energy and 0.05 eV/Å for force. A 15 Å vacuum layer was added in the z-direction to avoid the interaction between periodic images.

The binding energy (E_b) between two isolated systems can be calculated by the formula:

$$E_b = E_{AB} - E_A - E_B \quad (1)$$

where E_{AB} represents the total energy of the AB system. E_A and E_B are the energies of isolated A and B systems, respectively.

The adsorption energy (E_{ads}) was defined as:

$$E_{ads} = E_{total} - E_{sub} - E_{adsorbate} \quad (2)$$

where E_{total}, $E_{sub,}$ and $E_{adsorbate}$ are the total energies of the substrate with adsorbate, the substrate, and the free adsorbate, respectively.

RESULTS AND DISCUSSION

Effect of $BiCl_3$ additive on Mn deposition/stripping behavior and the Mn anode interface

Firstly, the chemical stability of the Mn anode in various electrolytes was evaluated. It is evident from Supplementary Figure 3 that the Mn anode demonstrated vigorous gas evolution upon immersion in the AE, whereas it remained stable in the nonaqueous counterparts (G2-$Mn(OTf)_2$ and G2-$BiCl_3$). This underscores the chemical incompatibility between the Mn anode and aqueous media, which precludes stable Mn deposition.

Electrochemical assessments in Mn||Mn symmetric cells further validated these results [Supplementary Figure 4]. At a current density of 0.1 mA cm^{-2}, the Mn||AE||Mn symmetric cell displayed a considerable polarization voltage of about 4 V and a limited cycle life of less than 40 h, primarily due to the parasitic HER. However, symmetric cells using G2-$Mn(OTf)_2$ and G2-$BiCl_3$ electrolytes exhibited excellent cycling stability of over 1,000 h [Figure 1A]. The G2-$BiCl_3$-based symmetric cells maintained stable voltage profiles without obvious short-circuiting or abrupt polarization growth during long-term cycling [Figure 1B, Supplementary Figure 5A]. To further evaluate the robustness of Mn plating/stripping under more

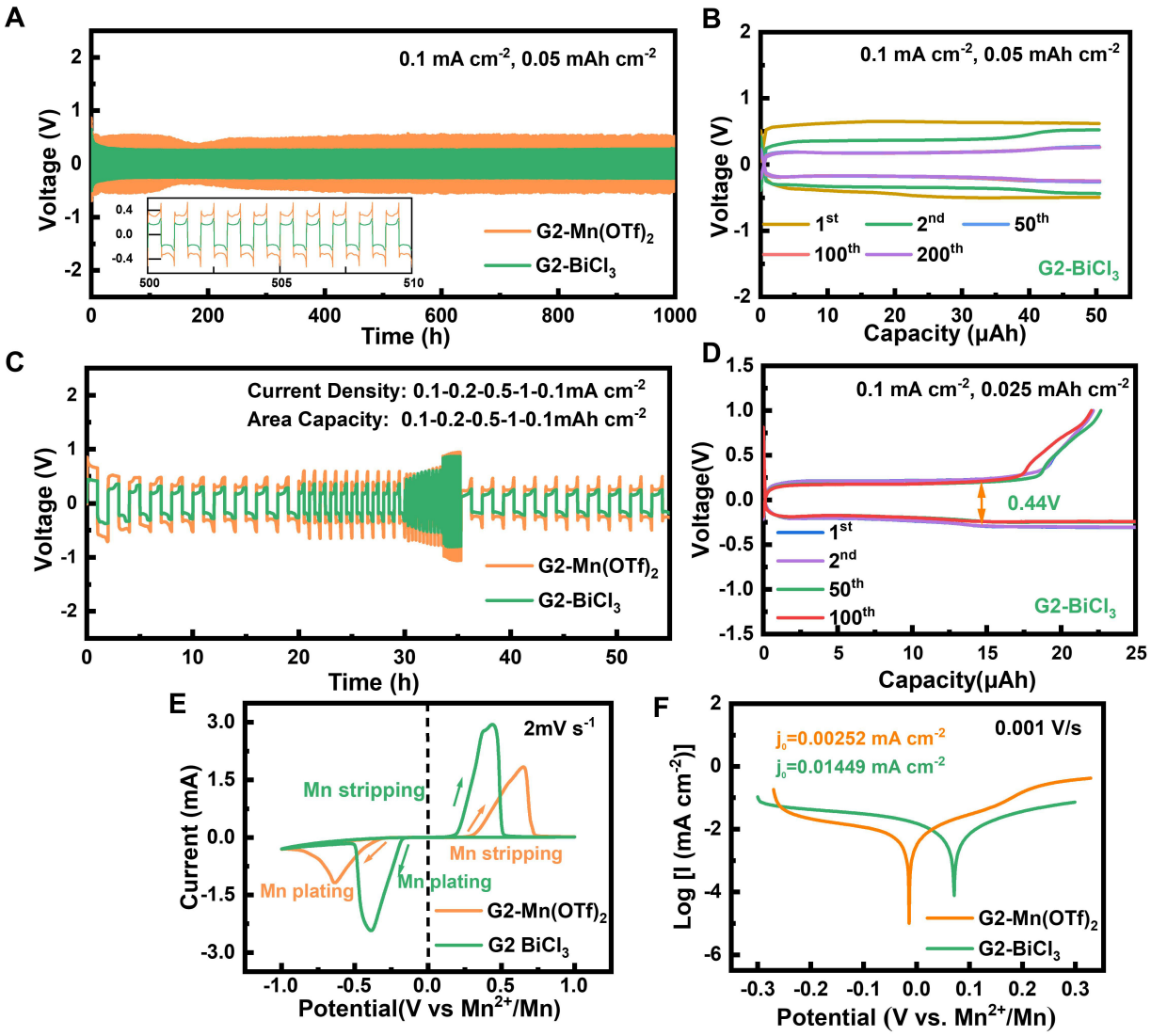

Figure 1. (A) Long-term cycling performance of Mn||Mn symmetric cells with different electrolytes; (B) Voltage profiles at selected cycles for the Mn||Mn symmetric cell using the G2-$BiCl_3$ electrolyte; (C) Rate capability of Mn||Mn symmetric cells with different electrolytes at various current densities; (D) Voltage profiles at designated cycles for the Mn||Cu half-cell using the G2-$BiCl_3$ electrolyte; (E) CV curves of the Mn||Cu half-cells with different electrolytes; (F) Tafel plots of pristine Mn anode and $BiCl_3$-modified Mn anode measured in a three-electrode configuration.

demanding conditions, additional symmetric cell tests were conducted at higher current densities and areal capacities [Supplementary Figure 6]. The G2-$BiCl_3$ electrolyte maintained stable cycling performance for over 1,000 h at 0.5 mA cm^{-2} with an areal capacity of 0.25 mAh cm^{-2}. Even under a higher current density of 1.0 mA cm^{-2} and an areal capacity of 0.5 mAh cm^{-2}, the G2-$BiCl_3$ electrolyte still enabled stable Mn plating/stripping for more than 1,000 h, corresponding to a cumulative plated capacity of approximately 500 mAh cm^{-2}. In contrast, the G2-$Mn(OTf)_2$ electrolyte exhibited pronounced polarization fluctuations and unstable voltage profiles under the same high-loading condition, indicating unstable Mn deposition/stripping behavior.

The overpotential of symmetric cells decreased significantly with $BiCl_3$ addition. Concentration-dependent studies [Supplementary Figure 7] indicated that 10 mM $BiCl_3$ was optimal, as a lower concentration (5 mM) was insufficient to reduce polarization, whereas the higher concentration (25 mM) showed an abrupt increase in overpotential at the end of cycling. The rate-capability measurements [Figure 1C] also showed the

kinetic benefits of the $BiCl_3$ additive. In G2-$BiCl_3$, no significant polarization was observed with an increase in current density, whereas in G2-$Mn(OTf)_2$, polarization was observed to increase with the rise in current density. Furthermore, the overpotential was restored to the initial level when the current density was reset back to 0.1 mA cm^{-2}, indicating good electrochemical reversibility and improved reaction kinetics.

To demonstrate the effect of $BiCl_3$ on Mn deposition, asymmetric cell cycling was carried out. Stable cycling was also achieved for Mn||Cu cells at 0.1 mA cm^{-2} and 0.025 mAh cm^{-2} over 100 cycles [Figure 1D, Supplementary Figure 5B]. However, a kinetic difference was found in CV [Figure 1E]. The strong coordination of Mn^{2+} with solvent molecules in the G2-$Mn(OTf)_2$ electrolyte may contribute to sluggish interfacial Mn deposition kinetics, resulting in a more negative onset potential of -0.32 V (*vs.* Mn^{2+}/Mn). This led to a deposition/dissolution overpotential of 1.29 V, corresponding to slow redox kinetics. The improved kinetics in the G2-$BiCl_3$ electrolyte are attributed to the $BiCl_3$ additive, which regulates the Mn anode interface and facilitates reversible Mn deposition and stripping.

The response current density and the integrated CV peak area of the symmetric cells [Supplementary Figure 8] indicated that $BiCl_3$ promoted the deposition/stripping activity. To quantitatively evaluate the interfacial redox kinetics of the Mn anode, exchange current density (j_0) measurements were further performed using a three-electrode configuration [Figure 1F]. The measurements were conducted in the G2-$Mn(OTf)_2$ electrolyte without $BiCl_3$ to exclude the direct contribution of $BiCl_3$ in the electrolyte. The $BiCl_3$-modified Mn anode exhibited a j_0 of 0.01449 mA cm^{-2}, approximately 5.75 times higher than that of the pristine Mn anode (0.00252 mA cm^{-2}), indicating substantially faster Mn^{2+}/Mn interfacial redox kinetics. This result is consistent with the enhanced deposition/stripping activity observed in the symmetric-cell measurements. These findings demonstrate that the $BiCl_3$ additive effectively improves the interfacial electrochemical kinetics of Mn deposition/stripping.

To elucidate the interfacial effects of $BiCl_3$ incorporation on the Mn anode, XRD was used to characterize the Mn anode surface after immersion. By-product Mn_3O_4 (PDF#18-0803) was formed after the immersion of the Mn anode in AE [Figure 2A], while the Mn anode in the G2-$Mn(OTf)_2$ electrolyte was still pristine [Figure 2B]. In the Mn anode in the G2-$BiCl_3$ system, however, clear diffraction peaks of Bi metal were found [Figure 2C]. These results suggest that a spontaneous interfacial reaction between Mn and Bi^{3+} species occurs during immersion, forming Bi-related species on the Mn surface ($3Mn + 2Bi^{3+} \rightarrow 3Mn^{2+} + 2Bi$). SEM and energy dispersive spectrometer (EDS) analyses further confirmed this surface change [Figure 2D-F, Supplementary Figure 9]. For the SEM/EDS immersion characterization, Mn powder was used to facilitate direct observation of the surface changes. The surface morphology of the Mn powder treated with G2-$BiCl_3$ electrolyte was evidently altered, and Bi was evenly distributed, suggesting the formation of Bi-containing surface species[33]. Furthermore, XPS and transmission electron microscope (TEM) characterizations were performed on the immersed Mn anodes to further investigate the chemical characteristics of the interfacial layer. The XPS results reveal the coexistence of Mn, Bi, O, and Cl elements within the interphase [Figure 2G]. The TEM images indicate that the interphase is predominantly amorphous [Figure 2H]. Meanwhile, the TEM-EDS elemental mapping further demonstrates that the Bi-containing interphase is relatively uniformly distributed over the Mn anode surface [Figure 2I]. Considering the strong diffraction signals of metallic Bi and the XPS evidence, metallic Bi is considered to be the predominant functional component within the Bi-containing interphase, although the coexistence of other species cannot be excluded. However, the exact chemical composition of this interphase cannot be unambiguously determined at this stage, as the species detected may originate from manganese oxides, bismuth oxides, chlorine-containing species, and/or other mixed interfacial components. Accordingly, this interfacial layer is referred to as a "Bi-containing interphase" throughout this work.

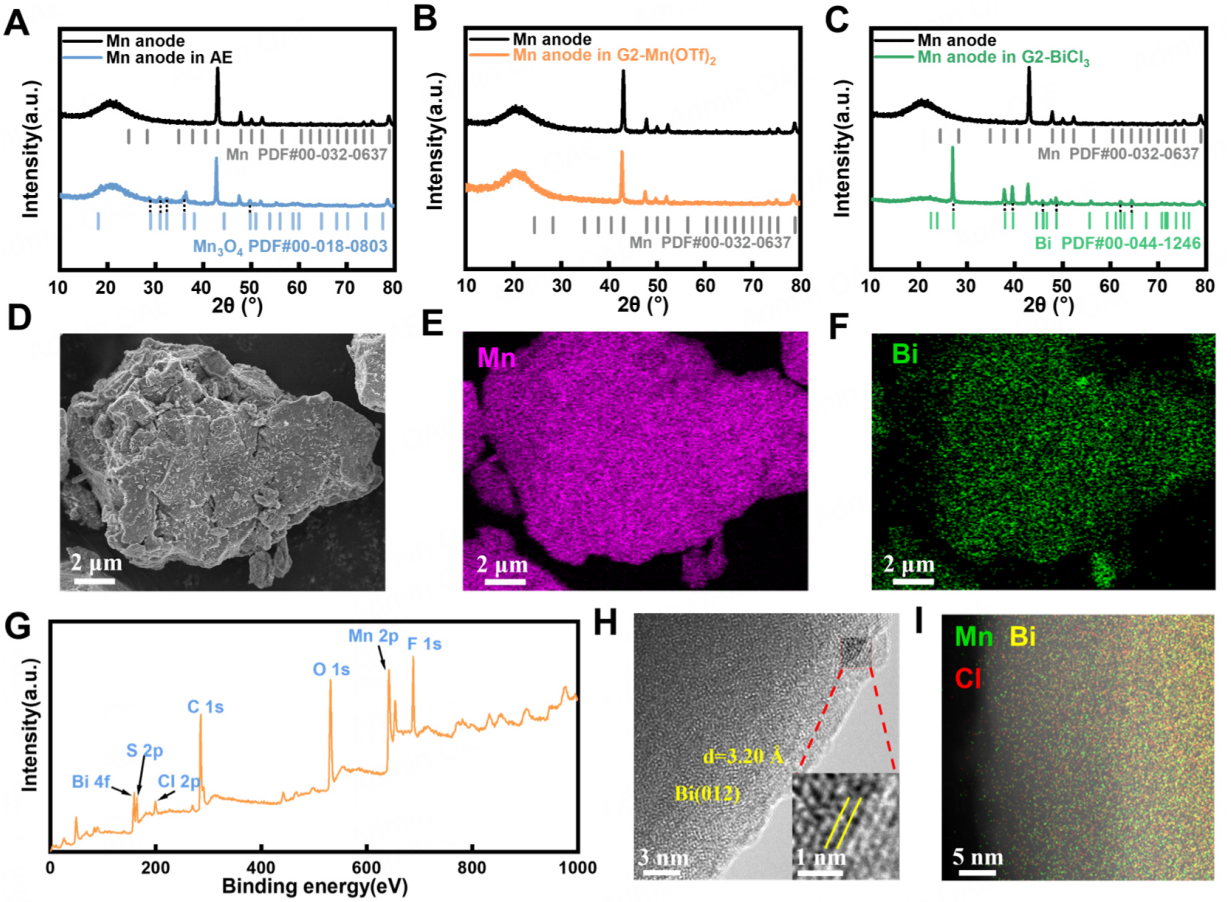

Figure 2. (A-C) XRD patterns of Mn anodes treated with different electrolytes; (D) SEM image and (E), (F) corresponding Mn and Bi EDS elemental mappings of Mn powder immersed in the G2-$BiCl_3$ electrolyte; (G) XPS survey spectrum of the Mn anode after immersion in the G2-$BiCl_3$ electrolyte; (H) TEM image and (I) corresponding EDS elemental mapping of the Bi-containing interphase on the immersed Mn anode.

Revealing the mechanism of $BiCl_3$ additive in enhancing reaction kinetics

Recent studies suggest that halogen atoms (X = Cl, Br, I), characterized by large ionic radii and low electronegativity, can reduce the coordination between Mn^{2+} and solvent molecules, reducing deposition overpotentials. Considering that $BiCl_3$ provides Cl atoms to the electrolyte, one hypothesis was that the kinetic advantages could be due to a halogen-mediated solvation effect. To investigate this, HRMS was performed on G2-$Mn(OTf)_2$ and G2-$BiCl_3$ electrolytes [Figure 3].

It is evident from Figure 3A and B that in the G2-$Mn(OTf)_2$ electrolyte, Mn^{2+} coordinates with G2 and OTf^- to form various cationic and anionic complexes, including $[Mn(G2)_2]^{2+}$, $[Mn_2(OTf)_3(G2)_2]^+$, $[Mn(OTf)_3]^-$, and $[Mn_2(OTf)_5]^-$. It is important to note that the mass spectrometry measurements for the G2-$BiCl_3$ electrolyte [Figure 3C and D] show that the most abundant species are the same as those found in the G2-$Mn(OTf)_2$ electrolyte, namely various cationic and anionic complexes formed between Mn^{2+}, G2, and OTf^-. Meanwhile, complexes directly formed between Bi^{3+} and Cl^- (e.g., $[BiCl_2(G2)]^+$ and $[Bi_2(OTf)Cl_4]^+$) are present only in trace amounts. These results show that the coordination environment of Mn^{2+} in the G2-$BiCl_3$ electrolyte is primarily governed by G2 and OTf^-, and that adding $BiCl_3$ has no significant effect on the dominant Mn^{2+} solvation structure. As additional support for refuting the halogen-mediated hypothesis, another control additive was selected, LiCl [Supplementary Figure 10]. In the cell with the electrolyte G2-LiCl (30 mM LiCl), no kinetic improvement was observed, although Cl^- was present in the electrolyte. Taken together, these results suggest that $BiCl_3$ primarily enhances the reaction kinetics by forming a Bi-containing interphase that

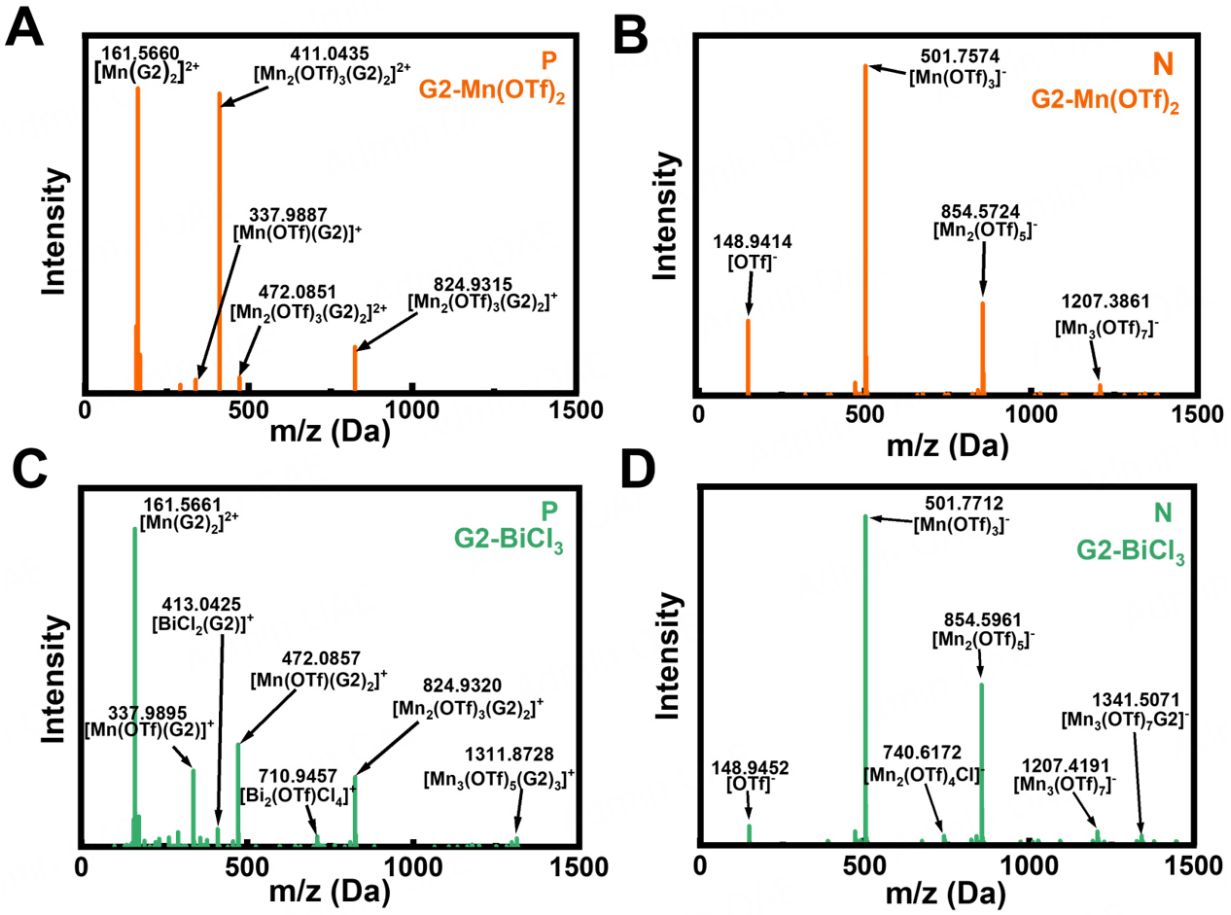

Figure 3. ESI-MS analysis of the different electrolytes. High-resolution ESI-MS spectra obtained in (A and B): G2-$Mn(OTf)_2$ electrolyte; (C and D): G2-$BiCl_3$ electrolyte. P/N denotes positive/negative ion mode, respectively.

regulates Mn deposition, rather than by significantly altering the dominant Mn^{2+} solvation structure, although a minor contribution from dissolved Cl-containing species to the local interfacial environment cannot be completely ruled out.

To explain the kinetic acceleration, DFT calculations and UPS characterization were carried out. The results obtained from the DFT calculations [Figure 4A and B] show that the adsorption energy of Mn atoms on the Bi(012) crystal plane is more negative than that on the Mn(411) plane. This stronger interaction between Mn species and the Bi surface suggests that the Bi-containing interphase may provide favorable adsorption sites, improve Mn adsorption and interfacial charge-transfer conditions, and consequently promote a more controlled Mn deposition process. Moreover, the work function (ϕ) of the Mn anode decreased from 4.45 eV in the G2-$Mn(OTf)_2$ electrolyte to 3.96 eV in the G2-$BiCl_3$ electrolyte, as determined by UPS analysis [Figure 4C-F]. The reduced work function suggests a modified surface electronic environment and a more favorable electronic structure for interfacial charge transfer, which may contribute to the enhanced interfacial redox kinetics.

To further understand the interfacial kinetic behavior, distribution of relaxation times analysis was performed based on the electrochemical impedance spectroscopy spectra. As shown in Supplementary Figure 11, the relaxation peaks can be assigned to different electrochemical processes, including solid electrolyte interphase (SEI)-related processes at high frequencies, charge-transfer processes at intermediate frequencies, and ion diffusion processes at low frequencies. Notably, a pronounced relaxation peak is

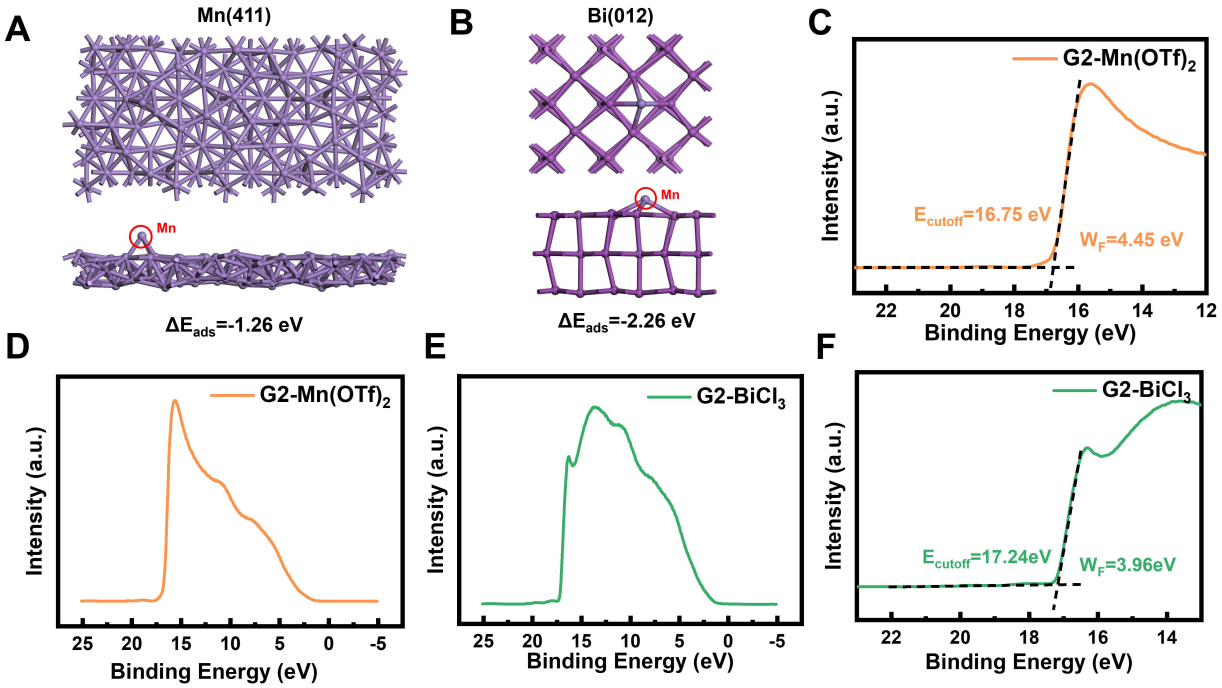

Figure 4. (A and B) Calculated adsorption energy of a Mn atom on Mn (411) and Bi (012) surfaces, respectively; UPS measurements of the work function of the (C), (D) Mn anode in G2-$Mn(OTf)_2$ electrolyte and (E), (F) Mn anode in G2-$BiCl_3$ electrolyte.

observed in the 10^{-4}-10^{-3} s region for the G2-$Mn(OTf)_2$ electrolyte, whereas no obvious relaxation peak is observed in this region for the electrolytes containing $BiCl_3$, including 5, 10, and 25 mM $BiCl_3$. Furthermore, among the $BiCl_3$-containing electrolytes, the 10 mM $BiCl_3$ electrolyte exhibits substantially lower charge-transfer resistance than those with 5 and 25 mM $BiCl_3$, indicating more favorable interfacial charge-transfer kinetics at the optimized $BiCl_3$ concentration. These results further support that the introduction of $BiCl_3$ facilitates more reversible Mn deposition/stripping and improves interfacial kinetics.

Based on these results, $BiCl_3$ acts as a multifunctional interfacial regulator, as shown in the schematic [Figure 5]. In the early stage of rest or in the initial stages of cycling, Bi^{3+} preferentially displaces surface Mn atoms to form a uniform Bi-containing interphase. This *in-situ* engineered interphase can work in several ways to optimize the Mn anode: (1) Improving interfacial kinetics: the Bi-containing interphase facilitates faster and more reversible Mn deposition/stripping processes; (2) accelerating the charge transfer: reduced surface work function can enhance the charge transfer rate at the electrochemical interphase; (3) protecting the interface: the Bi-containing interphase forms a good selective ion-conductor to block the formation of detrimental species such as Mn_3O_4, and ensures a high Mn^{2+} flux. To conclude, such a synergistic effect, both of strong atomic adsorption and favorable electronic structure, is an effective mechanism to overcome the slow redox reaction of the Mn anode and is an effective method for developing high-performance nonaqueous MIBs.

Electrochemical performance of Mn||$Cu_{1.8}S$ full cells

The practical effectiveness of the interface modified with $BiCl_3$ was investigated by synthesizing the cathode material $Cu_{1.8}S$ by a solvothermal process[35]. The successful preparation of $Cu_{1.8}S$ was confirmed by XRD, XPS, and SEM elemental mapping analyses [Supplementary Figure 12].

The effect of the $BiCl_3$ additive on the full-cell performance was systematically studied. The Mn||G2-$BiCl_3$||$Cu_{1.8}S$ cell delivered an average discharge capacity of 214.6 mAh g^{-1} over 100 cycles, which was higher than that of the Mn||G2-$Mn(OTf)_2$||$Cu_{1.8}S$ cell (158.0 mAh g^{-1}) at a current density of 20 mA g^{-1} [Figure 6A].

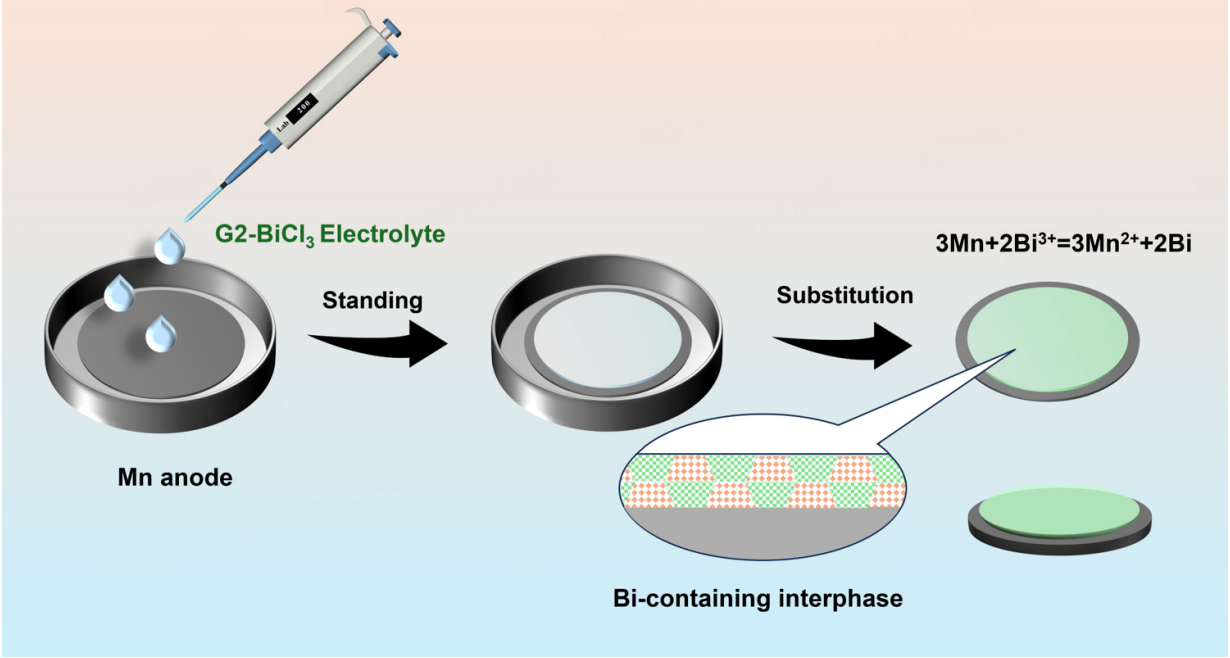

Figure 5. Graphical representation of the displacement reaction mechanism between Bi^{3+} and Mn in the G2-$BiCl_3$ electrolyte.

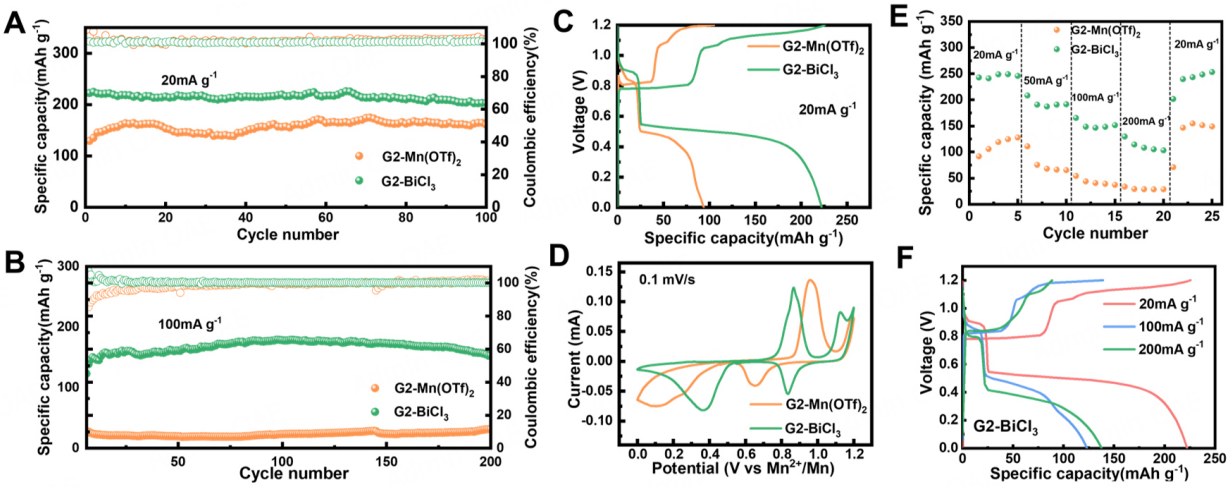

Figure 6. Electrochemical performance of Mn||$Cu_{1.8}S$ full cells with different electrolytes. (A) Long-term cycling performance at 20 mA g^{-1}, (B) Long-term cycling performance at 100 mA g^{-1}; (C) First-cycle charge/discharge profiles at a current density of 20 mA g^{-1}; (D) CV curves; (E) Rate capability at various current densities; (F) First-cycle charge/discharge profiles of the Mn||G2-$BiCl_3$||$Cu_{1.8}S$ full cell at different current densities.

Concentration-dependent studies [Supplementary Figure 13] showed that 10 mM $BiCl_3$ was optimal. When tested at a current density of 100 mA g^{-1}, the Mn||$Cu_{1.8}S$ cell with 10 mM $BiCl_3$ delivered an average discharge capacity of 166.1 mAh g^{-1} over 200 cycles, while maintaining almost 100% capacity retention after 200 cycles [Figure 6B]. These results are consistent with the symmetric cell findings. Moreover, the LiCl-based control cell [Supplementary Figure 14] showed no performance enhancement, reinforcing the conclusion that the kinetic gains are uniquely induced by the Bi-containing interphase rather than the presence of Cl atoms.

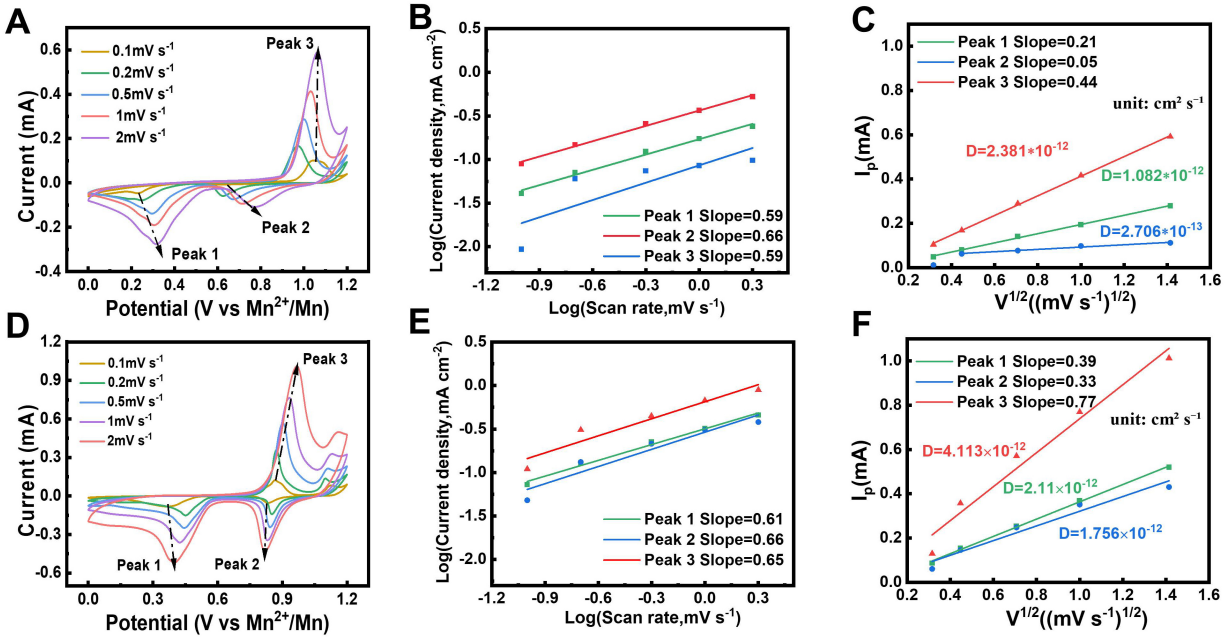

Figure 7. CV curves and kinetic analysis of Mn||$Cu_{1.8}S$ full cells in the G2-Mn$(OTf)_2$ and G2-$BiCl_3$ electrolytes. (A, D) CV curves at different scan rates; (B, E) Corresponding log(*i*) *vs.* log(*v*) plots used to determine the *b* values; (C, F) Peak current *vs.* $v^{1/2}$ plots used to calculate the Mn^{2+} diffusion coefficient (*D*, $cm^2\ s^{-1}$).

The GCD profile of the $Cu_{1.8}S$ cathode in both electrolytes is similar to the dual storage mechanism described in the literature [Figure 6C]. However, the most significant finding is the comparison of the profiles, showing that the $BiCl_3$ additive significantly reduces voltage polarization, one of the most important parameters in electrochemical processes. This kinetic enhancement was confirmed by CV, which showed that the G2-$BiCl_3$ system exhibited narrower peak separations and more distinct redox features [Figure 6D], indicating improved reaction reversibility and accelerated redox kinetics[36].

To understand how the $BiCl_3$ additive affects the full-cell kinetic characteristics, the rate capability of the full cells was measured [Figure 6E]. At current densities of 20, 50, 100, and 200 mA g^{-1}, the Mn||G2-$BiCl_3$||$Cu_{1.8}S$ cell demonstrates outstanding discharge capacities of 245.4, 193.6, 152.0, and 112.1 mAh g^{-1}, respectively. By comparison, the full cell with the G2-Mn$(OTf)_2$ electrolyte exhibits much lower capacities of 113.7, 77.1, 42.9, and 29.7 mAh g^{-1} at the same current densities. Further, by increasing the current density to 200 mA g^{-1} for long-term cycling stability testing [Supplementary Figure 15], the Mn||G2-$BiCl_3$||$Cu_{1.8}S$ full cell delivered an average specific capacity of 48.3 mAh g^{-1} over 800 cycles. In contrast, the cell with the G2-Mn$(OTf)_2$ electrolyte exhibited almost no measurable capacity under these high-current-density conditions. Furthermore, the first-cycle charge/discharge profiles at different current densities were analyzed [Figure 6F], demonstrating the stable charge/discharge behavior and good reversibility of the Mn||G2-$BiCl_3$||$Cu_{1.8}S$ full cell.

To quantify the charge-storage mechanism, a CV was carried out as a function of scan rate. The b-values ($i = av^b$) obtained for both electrolytes were found to be in the range 0.59-0.66, indicating that the electrochemical process is predominantly diffusion-controlled Figure 7). The calculated values of diffusion coefficients (D) for the G2-$BiCl_3$ system were significantly larger than those for the baseline, indicating that the Bi-containing interphase facilitates Mn^{2+} transport and charge transfer across the Mn/electrolyte interface. These results demonstrate that $BiCl_3$ effectively reduces interfacial kinetic limitations and enhances the electrochemical reaction kinetics of the Mn||$Cu_{1.8}S$ full cell.

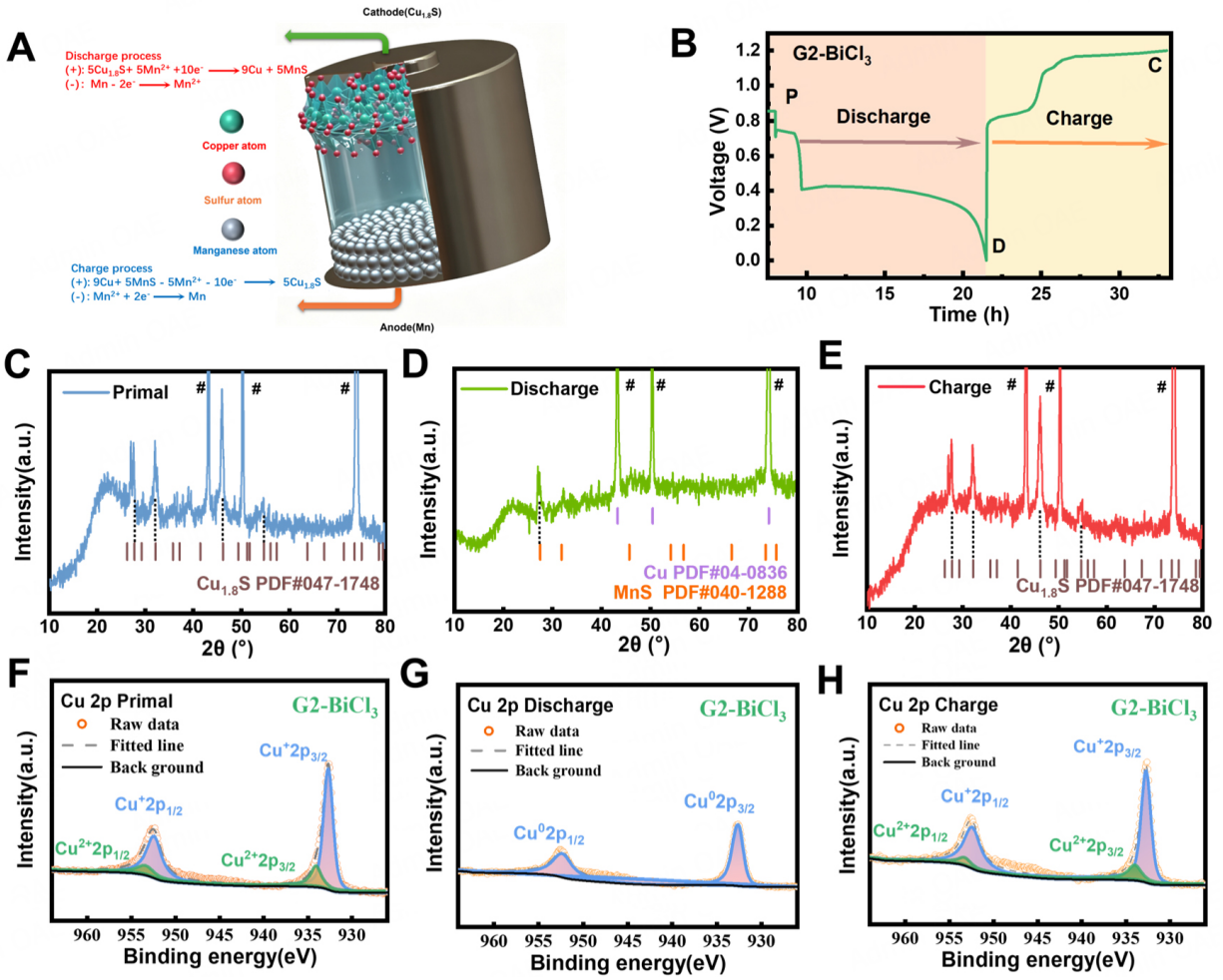

Figure 8. (A) Schematic representation of the internal conversion reaction mechanism in the Mn||$Cu_{1.8}S$ full cell; (B) Within the voltage range of 0 to 1.2 V, the GCD profile of the Mn||$Cu_{1.8}S$ full cell with G2-$BiCl_3$ electrolyte, indicating the states designated for *ex situ* measurements; (C-E) *Ex situ* XRD patterns, the # marks in the figure correspond to the XRD of the Cu current collector; (F-H) *Ex situ* XPS spectra of the Mn||$Cu_{1.8}S$ full cells at the corresponding states.

The schematic diagram of the Mn||$Cu_{1.8}S$ cell structure and its operation mechanism is shown in Figure 8A. At the anode, the Mn atoms are oxidized and enter the electrolyte in the form of ions Mn^{2+}. The electrons from the oxidation process at the anode travel to the cathode through the external circuit. At the cathode, Mn^{2+} and electrons react with $Cu_{1.8}S$ to yield MnS and metallic Cu *via* a displacement reaction. The charge process proceeds through the corresponding reverse electrochemical pathways.

Ex-situ XRD measurements of the cathodes were conducted at different electrochemical states during the first electrochemical cycle to track the phase evolution during cycling and to elucidate the role of $BiCl_3$ in cathode reactions and the resulting improvement in full-cell kinetics. Figure 8B and Supplementary Figure 16 show GCD curves of both cells with the two electrolytes, with the three sampling points of pristine (P), fully discharged (D), and fully charged (C). The *ex-situ* XRD results of the pristine state (P) indicate that the diffraction peaks of the cathode in both electrolytes match the $Cu_{1.8}S$ standard card [Figure 8C, Supplementary Figure 17A].

The phase evolution pathways of the two electrolytes are significantly different when the state of charge is fully discharged (D). The sluggish kinetics of the Mn anode cause severe polarization in the G2-$Mn(OTf)_2$ electrolyte, leading to the rapid onset of the cut-off condition and therefore premature end of the discharge

process, as shown by the presence of the $Cu_{1.8}S$ phases in the XRD pattern [Supplementary Figure 17B]. The latter G2-$BiCl_3$ electrolyte, in comparison, allows for the full conversion of the $Cu_{1.8}S$ cathode, with all of the primary diffraction peaks from $Cu_{1.8}S$ fully disappearing [Figure 8D]. At the same time, a comparison of the diffraction profiles in the fully discharged state (D) also shows a significant difference in the formation of the MnS reaction product. The characteristic peaks of the MnS phase are, in particular, more intense and well resolved for the G2-$BiCl_3$ electrolyte when compared to the G2-$Mn(OTf)_2$ electrolyte, which means that the transformation is more complete.

The difference in phase reversibility remains very large under fully charged conditions (C). The diffraction peaks corresponding to the discharge products MnS disappear entirely in the cell with the G2-$BiCl_3$ electrolyte, while the diffraction peaks of the $Cu_{1.8}S$ phase are completely recovered and restored [Figure 8E]. In contrast, the fully reconstructed $Cu_{1.8}S$ cathode in the baseline G2-$Mn(OTf)_2$ system was only partially reconstructed under standard conditions. The complete recovery of $Cu_{1.8}S$ in the electrolyte G2-$Mn(OTf)_2$ can only be realized when the charge voltage is raised to 1.3 V [Supplementary Figure 17C and D]. This requires a higher overpotential due to sluggish Mn anode interfacial kinetics, which hinder efficient Mn deposition/stripping processes. To further verify the different conversion behaviors, *ex situ* XPS analyses were also performed on the cathodes at the pristine (P), fully discharged (D), and fully charged (C) states [Figure 8F-H, Supplementary Figure 17E-G]. Notably, in the fully discharged state, the Cu 2p spectrum of the G2-$Mn(OTf)_2$ control still exhibits a detectable Cu^{2+} signal, indicating incomplete conversion of $Cu_{1.8}S$. In contrast, the Cu 2p spectrum of the G2-$BiCl_3$ cathode shows no detectable Cu^{2+} signal, with the Cu species predominantly converted to metallic Cu^0. These results provide additional chemical-state evidence for the more complete conversion of $Cu_{1.8}S$ in the G2-$BiCl_3$ electrolyte. Collectively, the XRD and XPS results indicate that the $BiCl_3$ additive regulates the Mn anode interface, reduces the interfacial kinetic polarization, and thereby facilitates more complete and reversible $Cu_{1.8}S$ conversion within the normal operating voltage range.

CONCLUSIONS

Here, we show how to improve the electrochemical properties of nonaqueous MIBs by rationally designing a $BiCl_3$-functionalized electrolyte. A kinetically active Bi-containing interphase layer was successfully engineered on the Mn anode by taking advantage of a spontaneous *in situ* galvanic displacement reaction, which enhances Mn deposition/stripping kinetics as supported by DFT calculations and UPS analysis. The resulting kinetic improvements lead to excellent electrochemical stability: symmetric Mn||Mn cells can be cycled for more than 1,000 h, and Mn||Cu1.8S full cells deliver an average discharge capacity of 166.1 mAh g^{-1} over 200 cycles at 100 mA g^{-1}. *Ex-situ* characterizations revealed that enhanced anode kinetics enable redox coupling throughout the cell, leading to a full and reversible phase change of the cathode material ($Cu_{1.8}S$) within a useful voltage range. This study not only introduces a high-performance technical solution but also provides a detailed understanding of the interfacial ion transport mechanism, which will serve as a solid basis for developing next-generation high-energy-density nonaqueous multivalent metal batteries.

DECLARATIONS

Authors' contributions

Writing - original draft, investigation, formal analysis: Zhang, Y. (Yuxuan Zhang); Zhang, Y. (Ying Zhang)
Methodology, Software, Validation, Formal analysis, Visualization: Liu, S.; Wuliji, H.
Writing - review & editing, conceptualization, supervision: Liu, H.; Bayaguud, A.

Availability of data and materials

Some results supporting this study are presented in the Supplementary Materials. Other raw data that support the findings of this study are available from the corresponding author upon reasonable request.

AI and AI-assisted tools statement

Not applicable.

Financial support and sponsorship

This work was supported by the National Natural Science Foundation of China (22301151), the National Key R&D Program of China (2023YFB2405800), and the Natural Science Foundation of Inner Mongolia Autonomous Region of China (2025MS02004).

Conflicts of interest

Bayaguud, A. is the Guest Editor of the special issue "Beyond Lithium-Ion Batteries: Materials and Mechanisms for Sustainable Energy Storage" of the journal *Energy Materials*. Bayaguud, A. was not involved in any stage of editorial processing, including reviewer selection, manuscript handling, and decision-making, while the other authors have declared that they have no conflicts of interest.

Ethical approval and consent to participate

Not applicable.

Consent for publication

Not applicable.

Supplementary Materials

Supplementary Materials

REFERENCES

1. Hu, S.; Pillai, A. S.; Liang, G.; et al. Li-rich layered oxides and their practical challenges: recent progress and perspectives. *Electrochem. Energy. Rev.* **2019**, *2*, 277-311. DOI
2. Xiong, F.; Tan, S.; Yao, X.; An, Q.; Mai, L. Crystal defect modulation in cathode materials for non-lithium ion batteries: progress and challenges. *Mater. Today.* **2021**, *45*, 169-90. DOI
3. Su, M.; Song, Y.; Xu, Q.; et al. Garnet conductor network with Zr doping to implement surface bifunctional modification for Ni-rich cathodes. *J. Energy. Storage.* **2024**, *95*, 112585. DOI
4. Li, C.; Zhang, X.; Zhu, Y.; et al. Modulating the lithiophilicity at electrode/electrolyte interface for high-energy Li-metal batteries. *Energy. Mater.* **2022**, *1*, 100017. DOI
5. He, Z.; Huang, Y.; Liu, H.; et al. Anode materials for fast charging sodium-ion batteries. *Nano. Energy.* **2024**, *129*, 109996. DOI
6. Usiskin, R.; Lu, Y.; Popovic, J.; et al. Fundamentals, status and promise of sodium-based batteries. *Nat. Rev. Mater.* **2021**, *6*, 1020-35. DOI
7. Tan, S.; Wen, Y.; Li, J.; et al. Fast-charging capabilities of hard carbon anodes in sodium-ion batteries: mechanisms, strategies, and prospects. *Carbon. Neutraliz.* **2025**, *4*, e70071. DOI
8. Li, M.; Lu, J. Ferric sauce for potassium-ion battery. *Nat. Sustain.* **2021**, *5*, 183-4. DOI
9. Dhir, S.; Wheeler, S.; Capone, I.; Pasta, M. Outlook on K-ion batteries. *Chem* **2020**, *6*, 2442-60. DOI
10. Niu, J.; Zhang, Z.; Aurbach, D. Alloy anode materials for rechargeable Mg ion batteries. *Adv. Energy. Mater.* **2020**, *10*, 2000697. DOI
11. Zhang, Z.; Cui, Z.; Qiao, L.; et al. Novel design concepts of efficient Mg-ion electrolytes toward high-performance magnesium-selenium and magnesium-sulfur batteries. *Adv. Energy. Mater.* **2017**, *7*, 1602055. DOI
12. Ming, J.; Guo, J.; Xia, C.; Wang, W.; Alshareef, H. N. Zinc-ion batteries: materials, mechanisms, and applications. *Mater. Sci. Eng. R. Rep.* **2019**, *135*, 58-84. DOI
13. Jin, X.; Song, L.; Dai, C.; et al. A self-healing zinc ion battery under -20 °C. *Energy. Storage. Mater.* **2022**, *44*, 517-26. DOI
14. Zhou, S.; Meng, X.; Chen, Y.; et al. Zinc-ion anchor induced highly reversible Zn anodes for high performance Zn-ion batteries. *Angew. Chem. Int. Ed.* **2024**, *63*, e202403050. DOI
15. Zhou, Y.; Wei, X.; Li, Y.; et al. Zincophilic vertically aligned hydrogel electrolyte with enhanced ion transport and dendrite suppression for stable zinc-ion batteries. *Carbon. Neutraliz.* **2026**, *5*, e70116. DOI
16. Zhang, E.; Cao, W.; Wang, B.; et al. A novel aluminum dual-ion battery. *Energy. Storage. Mater.* **2018**, *11*, 91-9. DOI
17. Li, C.; Hou, C.; Chen, L.; Kaskel, S.; Xu, Q. Rechargeable Al-ion batteries. *EnergyChem* **2021**, *3*, 100049. DOI

18. Nimkar, A.; Chae, M. S.; Wee, S.; et al. What about manganese? Toward rocking chair aqueous Mn-ion batteries. *ACS. Energy. Lett.* **2022**, *7*, 4161-7. DOI
19. Yang, Q.; Qu, X.; Cui, H.; et al. Rechargeable aqueous Mn-metal battery enabled by inorganic-organic interfaces. *Angew. Chem. Int. Ed.* **2022**, *61*, e202206471. DOI
20. Zheng, H.; Cheng, L.; Lu, W.; et al. An Mn^{2+} cross-linked gel electrolyte enables reversible quasi-solid-state manganese metal batteries. *Nano. Lett.* **2025**, *25*, 7716-24. DOI
21. Wang, M.; Meng, Y.; Xu, Y.; et al. Aqueous all-manganese batteries. *Energy. Environ. Sci.* **2023**, *16*, 5284-93. DOI
22. He, X.; Li, Z.; Tang, R.; et al. Rechargeable and highly stable Mn metal batteries based on organic electrolyte. *Chem. Commun.* **2023**, *59*, 1337-40. DOI
23. Yang, M.; Chen, R.; Shen, Y.; Zhao, X.; Shen, X. A high-energy aqueous manganese-metal hydride hybrid battery. *Adv. Mater.* **2020**, *32*, 2001106. DOI
24. Shen, D.; Zheng, X.; Luo, R.; et al. A rechargeable, non-aqueous manganese metal battery enabled by electrolyte regulation. *Joule* **2024**, *8*, 780-98. DOI
25. Fan, W.; Liu, F.; Liu, Y.; et al. A high voltage aqueous zinc–manganese battery using a hybrid alkaline-mild electrolyte. *Chem. Commun.* **2020**, *56*, 2039-42. DOI
26. Luo, H.; Guo, H.; Li, X.; et al. Aqueous manganese-ion batteries: the past, present, and future. *Matter* **2025**, *8*, 102379. DOI
27. Hou, Z.; Lu, W.; Zheng, H.; et al. An Mn-enriched interfacial layer for reversible aqueous Mn metal batteries. *Nano. Lett.* **2024**, *24*, 14034-41. DOI
28. Zhang, J.; Chen, F.; Yu, J.; et al. Asymmetric Mn^{2+} cluster electrolyte for high-performance Mn-metal batteries. *Adv. Funct. Mater.* **2025**, *36*, e15536. DOI
29. Jing, P.; Zhou, Y.; Liu, Y.; et al. Deciphering Mn^{2+} solvation and interfacial chemistry for rechargeable nonaqueous Mn-metal batteries. *Angew. Chem. Int. Ed.* **2025**, *64*, e202515941. DOI
30. Liu, R.; Yu, L.; He, X.; et al. Constructing heterointerface of Bi/Bi_2S_3 with built-in electric field realizes superior sodium-ion storage capability. *eScience* **2023**, *3*, 100138. DOI
31. Zhang, J.; Lu, X.; Li, M.; Sun, Z. Application of porous bismuth-based materials in sodium ion batteries. *Chem. Commun.* **2025**, *61*, 13616-31. DOI
32. Huang, J.; Lin, X.; Tan, H.; Zhang, B. Bismuth microparticles as advanced anodes for potassium-ion battery. *Adv. Energy. Mater.* **2018**, *8*, 1703496. DOI
33. Chen, H.; Zhang, W.; Yi, S.; et al. Zinc iso-plating/stripping: toward a practical Zn powder anode with ultra-long life over 5600 h. *Energy. Environ. Sci.* **2024**, *17*, 3146-56. DOI
34. Bi, J.; Li, J.; Zhou, Z.; et al. In situ formation of a Bi/Mg-based hybrid interphase for highly reversible magnesium metal anodes. *Adv. Mater.* **2025**, *37*, 2502098. DOI
35. Shen, D.; Zhao, G.; Jiang, T.; et al. A high-capacity manganese-metal battery with dual-storage mechanism. *Angew. Chem. Int. Ed.* **2025**, *64*, e202423921. DOI
36. Yin, H.; Wu, H.; Yang, Y.; et al. Electrical double layer and in situ polymerization SEI enables high reversible zinc metal anode. *Small* **2024**, *20*, 2404367. DOI